Received: 29 January 2018 | Revised: 29 January 2019 | Accepted: 30 January 2019 | Published on: 11 March 2019

DOI: 10.1002/qj.3496

RESEARCH ARTICLE

Quarterly Journal of the Royal Meteorological Society RMetS

A numerical simulation of a strong wind event in January 2013 at King Sejong station, Antarctica

Hataek Kwon[1] | Sang-Jong Park[1] | Solji Lee[1] | Baek-Min Kim[2] | Taejin Choi[1] | Seong-Joong Kim[1]

[1]Division of Polar Climate Science, Korea Polar Research Institute, Incheon, South Korea
[2]Department of Environmental Atmospheric Sciences, Pukyong National University, Busan, South Korea

Correspondence
Seong-Joong Kim, Korea Polar Research Institute, 26 Songdomirae-ro, Yeonsu-gu, Incheon 21990, South Korea.
Email: seongjkim@kopri.re.kr

Funding information
Korea Polar Research Institute, PE19010.

A strong wind event (SWE), so-called "severe gale", with a 10 min average wind speed of above 22 m/s occurred on 7 January 2013 at the King Sejong station (KSJ) on the tip of the Antarctic Peninsula (AP). We examine the cause of the SWE and assess the short-term predictability of such an event, using the state-of-the-art Polar Weather Research and Forecasting (Polar WRF) model. The simulation results, initialized at 0000 UTC 6 January 2013, the day prior to the occurrence of the SWE, produce the most accurate representation of the SWE in terms of strength (~94% of the peak wind speed). Both model results and observational records reveal that the SWE is mainly caused by the approach of a deep depression with the central pressure of 950 hPa. On top of this synoptic configuration, a particular shape of topography of the AP plays a non-negligible role for further intensification of the wind at KSJ. As the cyclone approaches the AP, the sea-level pressure becomes lower and is deformed around the AP due to the topography, driving southeasterly winds traversing the AP. The continuous flow overriding the AP generates a downslope windstorm at the lee side of the AP. The windstorm effect driven by the deformation of sea-level pressure by the topography of the AP is not properly represented in the coarser-resolution (27 km) model domain compared with higher (3 and 9 km) resolutions. We conclude that the SWE at KSJ on 7 January 2013 is caused by the combined effect of a synoptic-scale low-pressure system with local topography of the AP.

KEYWORDS
Antarctic Peninsula, depression, Polar WRF, strong wind event

1 | INTRODUCTION

A strong, sustained near-surface wind is one of the most prominent features of the Antarctic climate system and has been studied in observational (Turner *et al.,* 2001; 2009), theoretical (Ball, 1960; Parish and Bromwich, 1987), and numerical modelling (Parish and Waight, 1987; Heinemann, 1997; Adams, 2005; Orr *et al.,* 2014; Deb *et al.,* 2016) analyses. Due to the effect of katabatic flow from the continental interior towards the coast, studies on strong wind have been conducted for coastal regions of Antarctica, especially for East Antarctica. These studies have shown that many of the strong wind events observed over the Antarctic coasts are caused by either the persistence of topographic effects arising from strong katabatic wind, or synoptic-scale depressions that travel just off the Antarctic coastal region (Simmonds and Keay, 2000), and sometimes the combined effect of these two is responsible for the severe weather (Parish and Bromwich, 1998; van den Broeke and van Lipzig, 2003; Turner *et al.,* 2009).

Not all sectors of the Antarctic Peninsula (AP) experience persistent katabatic winds, although their climates are strongly influenced by the local orography. The AP is highly influenced by deep cyclonic systems from the Bellingshausen Sea that pass through the Drake Passage because it is located at the latitude of the circumpolar trough (Turner *et al.,* 2009). Therefore, severe weather events, such as strong winds and blizzards, often occur around the AP. However,

very few previous studies have investigated severe weather events in this region. Turner *et al.* (2009) examined the characteristics of strong wind events over the AP using *in situ* meteorological observations at the Bellingshausen and Faraday stations and concluded that the strong wind events over the AP were strongly influenced by synoptic-scale depressions in its vicinity. Notwithstanding Turner *et al.* (2009)'s work, there is still a lack of comprehensive understanding on severe weather events over the AP. Although there are reanalysis data available, limitations exist in carrying out an analysis of small-scale extreme weather events at relatively low resolution, in comparison to a regional model. Thus, a high-resolution regional-scale atmospheric model is an appropriate tool to generate fine-scale, dynamically and physically consistent regional-scale fields found in observations (Giorgi *et al.,* 1994).

In this study, we examine a strong wind event that occurred on 7 January 2013 at the King Sejong station (hereinafter called "KSJ") located in the AP, using the Polar Weather Research and Forecasting (Polar WRF) model (Hines and Bromwich, 2008). The strong wind event occurring in austral summer (January) is unusual and remarkable because wind is relatively calm at KSJ during austral summer. There have been only two strong wind events exceeding instantaneous wind speed 41 m/s during summer since the establishment of KSJ. The instantaneous wind speed of about 41 m/s recorded in this case is the second biggest value in January. The observed 10 min average wind speed of about 22 m/s is classified as severe gale force on the Beaufort wind scale.

Sensitivity experiments on the initialization time of the model are carried out, following the previous study where changing the initialization time produced the largest sensitivity for strong wind simulations at Mawson, East Antarctica (Orr *et al.,* 2014). With this information, we first evaluate the performance of the Polar WRF model by comparing the strong wind reproduced in the model with local surface observations. We also discuss the main cause of the strong wind event observed at KSJ by analysing the observations and numerical simulation results.

Section 2 describes data, model experiments and validation methodology. General characteristics of strong wind distribution at KSJ follow in section 3. Sections 4 and 5 present the case description, simulation results and possible mechanism of the strong wind event at KSJ, respectively.

2 | DATA AND METHODS

2.1 | Data

Surface observations from the Automatic Meteorological Observation System (AMOS-1) in operation at KSJ for 27 years from 1989 to 2015 are analysed in this study. The AMOS comprises a wind vane and an anemometer installed at a height of 10 m; a thermo-hygrometer at an elevation of about 2 m; and a rain-gauge and a barometer at about 1.5 m above the ground (Park *et al.,* 2013). The data measured by each sensor at an interval of 10 s or 1 s, depending on the parameter of interest, are averaged once every 10 min and stored in the data recorder.

Daily and monthly mean data derived from 10 min average observations of 10 m wind speed and direction are used for the climatological analysis. In December 2003, a backup observation system (AMOS-2) was installed and commissioned at a location 5 m from AMOS-1. For our analysis, the surface observations obtained from AMOS-1 are the primary dataset and any missing date periods are supplemented by AMOS-2 data. In this study, AMOS-2 data have been used for 2005, 2006, 2007 and 2008, when many of the AMOS-1 data are missing. Surface variables from AMOS-1 and AMOS-2 are compared (not shown) for May and September 2008 in order to demonstrate their consistency. Comparison of daily mean values of 10 m wind from AMOS-1 and AMOS-2 shows a good agreement, with a mean difference of 0.3 m/s (for u component of 10 m wind) and −0.5 m/s (for v component of 10 m wind). The root-mean-square errors are 1.25 m/s (for u component of 10 m wind) and 2.2 m/s (for v component of 10 m wind). In addition, to confirm the quality of the surface meteorological observations that are used, we also compare them to the monthly surface station data from the Reference Antarctic Data for Environmental Research (READER) database (http://www.antarctica.ac.uk/met/READER/metadata/metadata.html) created by the Scientific Committee on Antarctic Research (SCAR) (Turner *et al.,* 2004). Note that the monthly mean values provided by READER are produced as the mean of the 6-hourly synoptic observations. Comparison of yearly mean values of 10 m wind from 1994 to 2015 shows good agreement between the datasets. The mean differences in the yearly mean of 10 m wind between our data and the READER metadata are −1.95 m/s and −1.06 m/s for the u and v components of the 10 m wind, respectively. The 6-hourly European Centre for Medium-range Weather Forecasting (ECMWF) Interim reanalysis (ERA-Interim: Dee *et al.,* 2011) data (equivalent to a resolution ∼0.75°) are compared with the daily climatological trends of 10 m wind speed derived from AMOS data discussed in section 3.

2.2 | Model description

The Polar WRF (Hines and Bromwich, 2008) model (version 3.7), which is a modified version of the Advanced Research WRF (ARW; WRF-ARW: Powers *et al.,* 2017) that better represents key regional physical processes over the polar regions, is used for the simulation of the strong wind event at KSJ. The main modifications of the Polar WRF are included in the Noah Land Surface Model (Hines and Bromwich, 2008), which improves the representation of heat transfer through snow and ice. For the numerical simulation of the strong wind event, we apply three model domains with a horizontal resolution of 27, 9 and 3 km around King George Island, where

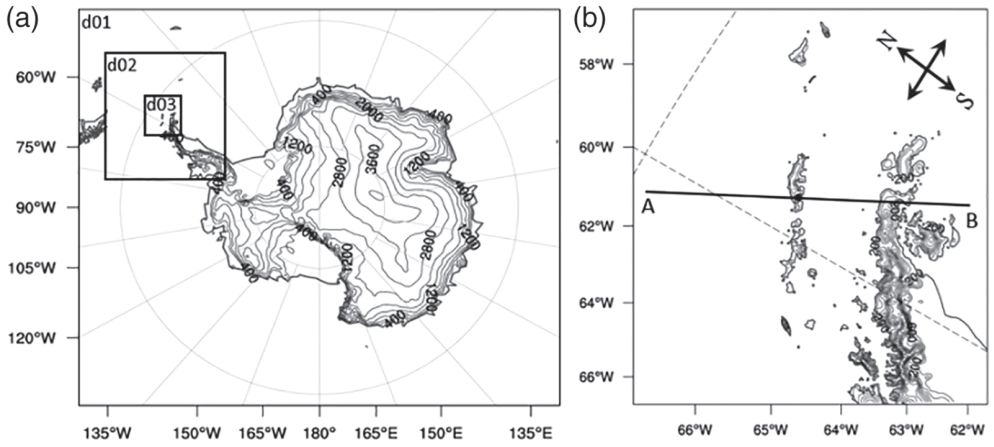

FIGURE 1 (a) Model domain at horizontal resolutions of 27 (d01), 9 (d02), and 3 (d03) km with terrain heights (contours, m). (b) Enlarged view of the 3 km domain (d03), where the King Sejong station is located (black circle). The contour intervals of elevation in (a) and (b) are 400 and 200 m, respectively. The black line from A to B represents the location of the vertical cross-section used in this study

KSJ is located (Figure 1). The 27 km domain covers the entire Antarctic continent, and the 9 and 3 km domains cover progressively smaller regions of the AP sector that encompasses King George Island. Three model domains are organized as two-way nesting; the top of the model is set to 10 hPa, with 61 vertical layers, starting at approximately 13 m above the surface. The ERA-Interim reanalysis data with a horizontal resolution of ∼0.75° are used as the initial and boundary conditions for the model simulation. The physics options used in this study refer to the previous studies evaluating the simulation performance of the WRF for the Antarctic region by Bromwich *et al.* (2013). The physical parametrizations used in the experiment include the WRF Single Moment 5-Class cloud microphysics scheme (Hong *et al.,* 2003), the Noah land surface model (Chen and Dudhia, 2001), and the new version of the rapid radiative transfer models (Iacono *et al.,* 2008) for general circulation models (RRTMG) for both short-wave and long-wave radiation. The Mellor–Yamada–Janjić turbulent kinetic energy (TKE) scheme (Janjić, 1994) is used for the planetary boundary-layer parametrization and the Monin–Obukhov (Monin and Obukhov, 1954) scheme is used for the surface layer. The Grell–Devenyi ensemble scheme (Grell and Devenyi, 2002) is applied to the 27 km grid domain alone for the cumulus convective parametrization. The detailed information about the model set-up is summarized in Table 1. The land-type and topography information obtained from the default United States Geological Survey 24-category land-use data and global 30″ elevation data (GTOPO30) are used for the model run. The actual topographic height at KSJ, located on the coast, is as low as 10 m. On the other hand, the model terrain height at the nearest grid point for each domain is 69.3 m (27 km), 40.1 m (9 km) and 0 m (3 km), which differ significantly from the actual topographic height. Note that, although KSJ is located on the shore of a small island, the actual and model terrain height of the 3 km spatial resolution grid show relatively good agreement with a difference value of about 10 m.

2.3 | Model experiments and validation methodology

To examine the sensitivity to the initialization time of the model, the Polar WRF models are initialized at different times and integrated for the selected period from 0000 UTC 6 January to 0000 UTC 9 January 2013. Orr *et al.* (2014) showed that the model simulation is very sensitive to moving the initial time for their strong wind event simulation at Mawson, East Antarctica. Each model simulation is initialized at 0000 UTC every day from 1 to 6 January using ERA-Interim reanalysis data and run forward until 0000 UTC on the 9th to simulate the strong wind event that occurred on 7 January. That is, six model simulations with different initialization times are run. The model simulations are specified as "jan6", "jan5", "jan4", "jan3", "jan2" and "jan1" in this article. An additional experiment is performed to see the effect of considering spin-up time for the strong wind simulation. In this experiment, the 48 h time integration is carried out after initializing at 0000 UTC every day and the first 24 h simulation result is excluded, taking into account the spin-up, and only that of the remaining 24 h results (24–48 h of the model output) are combined into simulation results for the analysis. This experiment is specified as "s24h". All numerical experiments are illustrated in the schematic diagram shown in Figure 2.

The strong wind simulation performance of the Polar WRF is evaluated by comparing model output with near-surface meteorological variables observed at KSJ. The nearest model grid value to the observation point is used in the comparison. Since the model output is an instantaneous value, in principle, it should be properly time-averaged to compare with the averaged observation. However, we found that the comparison results are not sensitive to the particular choice of time-averaging period up to 1 h (not shown). In this study, we present the results using hourly mean observations to compare with the model results. Note that height correction for a difference between model and real topography is not applied in the comparison. The hourly mean values are obtained by averaging observations at 10 min intervals. The 10 m wind speed and direction, 2 m temperature and sea-level pressure

TABLE 1 Summary of model configuration

	Domain1	Domain2	Domain3
Horizontal grid	281 × 242	202 × 220	187 × 205
Resolution	27 km	9 km	3 km
Vertical layers	61 layers (model top: 10 hPa)		
Geog data resolution	10 m′	30 s′	30 s′
Initial, lateral boundary condition	ERA-Interim (6 h intervals with a spatial resolution of 0.75° × 0.75°)		
Time period	0000 UTC 6th–0000 UTC 9th January 2013		
Base state temperature	273.16 K		
Relaxation zone	4 grid point (default)		

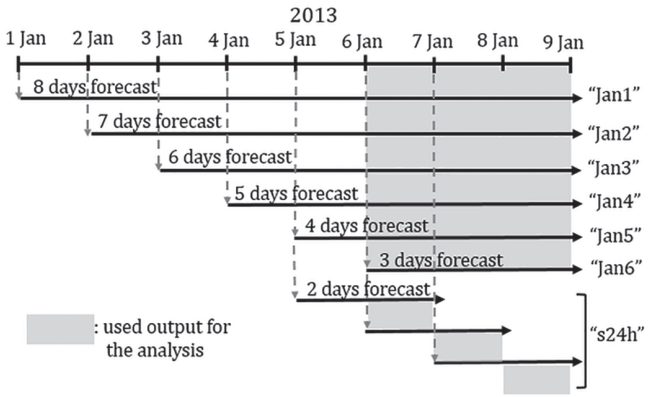

FIGURE 2 Time table of sensitivity experiments with different initialization times. The grey zone indicates the analysis period that is used for each experiment

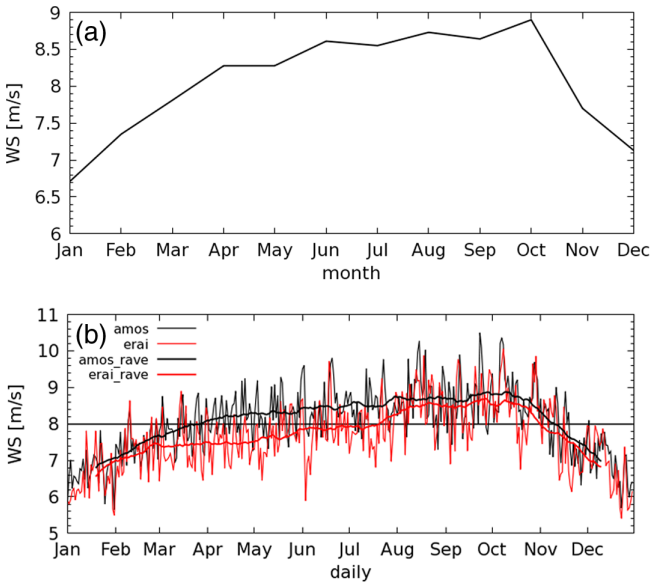

FIGURE 3 (a) Monthly and (b) daily climatology of wind speed (m/s) from observations (black thin line) and reanalysis (thin grey line) at KSJ station for the period 1989–2015. The bold black and red lines indicate the moving average value of daily variations in wind speed from observation and reanalysis data, respectively [Colour figure can be viewed at wileyonlinelibrary.com].

derived from surface pressure are used to validate the model results.

3 | CHARACTERISTICS OF STRONG WIND DISTRIBUTION AT KSJ STATION

Surface meteorological variables including surface air temperature, wind speed and sea-level pressure at KSJ typically show a weak seasonal cycle throughout the year. Especially, monthly-mean wind speeds exhibits small differences of about 2–3 m/s (Figure 3a), which is consistent with the wind observations at the Bellingshausen Station (62.2°S, 58.9°W), located near KSJ (Turner *et al.,* 2009; van Wessem *et al.,* 2015). Year-round frequent passage of low-pressure systems is regarded as a contributing factor for this weaker seasonal cycle (Simmonds and Keay, 2000; Turner *et al.,* 2009). For this region, northwesterly winds (annual mean value of ∼345°) prevail throughout the year (not shown). Figure 3b shows daily climatology of wind speed at KSJ during the period from 1994 to 2015. The daily mean wind speed exceeds 8 m/s from mid-autumn (April) to spring (October). Notable peak values of daily wind speed are found in August, when the storm activity around Antarctica is most pronounced, and in October with the southward migration and deepening of the circumpolar trough as a result of the semi-annual oscillation (Meehl, 1991; Simmonds and Jones, 1998). Wind speed starts to decrease from mid-October and becomes weakest in summer with a value of about 4.8 m/s. Figure 3b also shows wind speed climatology obtained from ERA-Interim data (red). The climatological wind in ERA-Interim data is reasonably consistent with observations in the warm season with a small negative bias. Note, however, that in the cold season, when wind becomes stronger, ERA-Interim underestimates wind speed much more.

As described in the introduction, the strong wind event occurred on 7 January 2013 with daily mean wind speed of about 16 m/s. Therefore, as an anomaly, the event is obviously extreme and unusual compared to the climatological wind of about 6.7 m/s in summer. To evaluate the degree of extremeness of our case quantitatively, we show the frequency distribution of the daily mean and 10 min average wind speed for the period from 1989 to 2015 and the daily maximum instantaneous wind speed for the period from 2005 to 2015, respectively (Figure 4). Comparing the wind speeds of this event with the distribution of climatological winds illustrates

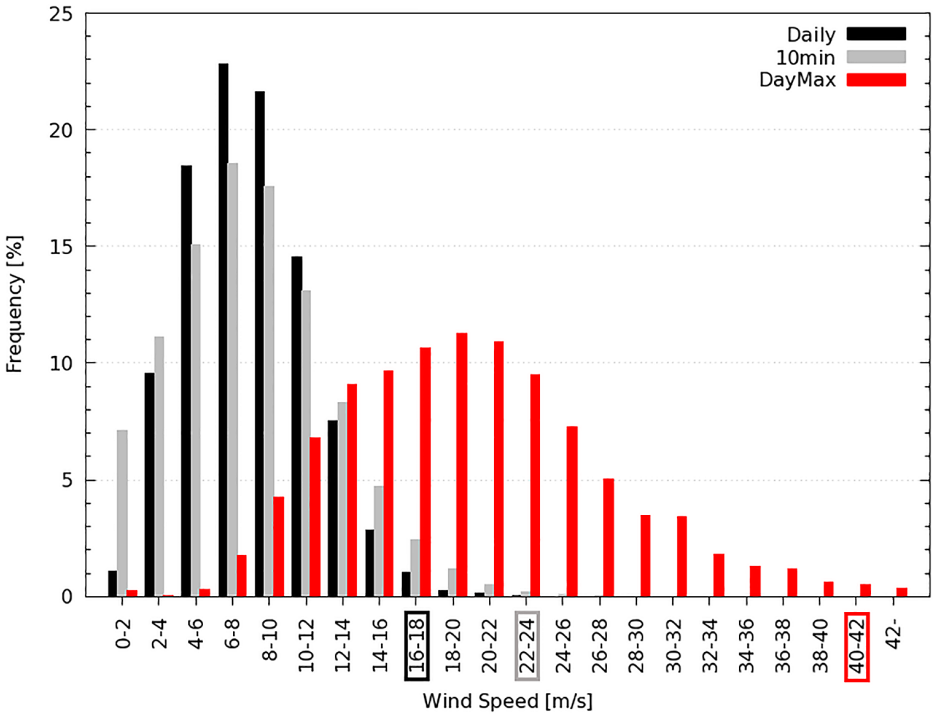

FIGURE 4 Frequency distribution of 10 min (grey) and daily averaged (black) for 1989–2015, and daily maximum value of instantaneous 10 m wind speed (red) for 2005–2015. The boxes on the *x*-axis correspond to the observed records of the event for daily averaged (black), 10 min (grey), and daily maximum value of instantaneous 10 m wind speed (red) [Colour figure can be viewed at wileyonlinelibrary.com].

how extreme the event is. The boxes on the *x*-axis of Figure 4 correspond to the observed values of the event. Daily mean values of 16 m/s (black box) occur less than 3% of the time; 10 min average values of 22 m/s (grey box) occur less than 0.34% of the time; daily maximum instantaneous winds of 41 m/s (red box) occur less than 0.88% of the time.

To examine the characteristics of extreme wind events at KSJ, we present wind direction and composite map of mean-sea-level pressure for extreme cases exceeding 41 m/s of maximum instantaneous wind speed (Figure 5). The 22 strong-wind cases are divided into two groups of major wind direction: easterly (90–150°, 13 cases) and northerly (326–360°, 0–33°, 9 cases). The composite map of mean sea-level pressure is prepared using 6-hourly ERA-Interim data at times close to the maximum instantaneous wind speed. Composite maps present a well-developed low-pressure system over Drake Passage. The central location and scale of low-pressure systems are different in each of the two cases. The pressure pattern is consistent with the major wind direction at KSJ, which is placed at the margin of the cyclone near the strong pressure gradient. This suggests the controlling role of low-pressure systems passing by Drake Passage on strong winds observed at KSJ.

4 | CASE DESCRIPTION

4.1 | The synoptic environment

To review the synoptic conditions for the selected strong-wind case, we present the surface weather charts provided by the Chilean Meteorological Office. Figure 6 shows the distribution of surface pressure for the period from 6 to 8 January 2013. The low-pressure system directly related to the strong wind event is generated at the southern end of Chilean territory on 6 January during the passage of a preceding large low-pressure system moving from west to east (Figure 6a,b). Subsequently, the newly generated low-pressure system moves toward the southeast direction, deepening the central pressure with time, and arrives in the vicinity of KSJ on 7 January; surface pressure shows the value of about 965–970 hPa and isobars are densely distributed over the surroundings of KSJ at 1800 UTC 7 January (Figure 6c). Note that the pressure pattern shows large similarity with the composite mean sea-level pressure map in Figure 5b, contributing to the strong easterly wind observed at KSJ. Though the low-pressure system is still located near KSJ on 8 January (Figure 6d), the intensity becomes weaker (with the surface pressure value of about 970–975 hPa) than that on 7 January. Consistently, the wind speed at KSJ has greatly decreased. The weakened low-pressure system moves far to the east after 1800 UTC 8 January (not shown).

4.2 | Surface observations

The strong wind event occurring at KSJ on 7 January 2013 lasts almost 12 h, from 0640 to 1850 UTC and is recorded as a blizzard in the weather report, the criteria being a wind speed in excess of 14 m/s with heavy snow, and visibility below 150 m. From AMOS observations (Figure 7a), the hourly mean wind speed is around 10 m/s on 6 January and

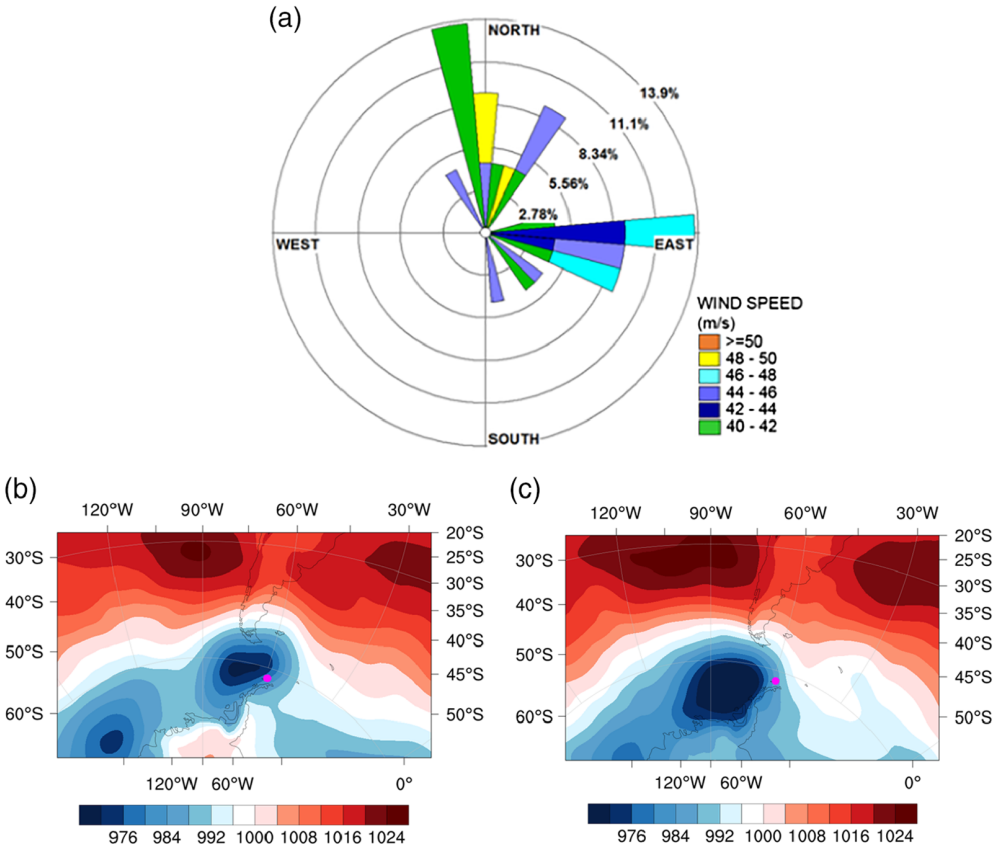

FIGURE 5 (a) Wind rose diagram of maximum instantaneous wind speed exceeding 41 m/s at KSJ station. Composite mean-sea-level pressure (hPa) of strong-wind cases showing (b) easterly and (c) northerly wind, respectively. Filled circles indicate the KSJ station [Colour figure can be viewed at wileyonlinelibrary.com].

then starts to rapidly increase at 0000 UTC 7 January until it reaches its maximum of about 21 m/s at 0800 UTC 7 January. This strong wind continues until around 1800 UTC 7 January, during which time it shows a maximum instantaneous wind speed exceeding 41 m/s. Subsequently, the wind speed gradually decreases and remains at around 5 m/s after 0600 UTC 8 January.

During the selected event, the wind direction varies from about 100 to 150°, showing mainly a southeasterly direction (Figure 7d). Note that the northwesterly wind generally prevails in January at KSJ. The surface pressure shows changes in opposite phase to the change in wind speed (Figure 7b). The surface pressure is shown to be around 978 hPa throughout 6 January, and it begin to decrease around 0000 UTC 7 January, when the wind speed begins to increase, and drops to around 965 hPa at 0800–0900 UTC 7 January, when the maximum hourly wind speed is observed at KSJ. The lowest surface pressure, of about 961 hPa, is recorded during 1600–1800 UTC 7 January, when the highest value of maximum instantaneous wind speed of about 41 m/s occurs. The surface temperature decrease during the period of strong wind (Figure 7c) is thought to be due to cold air advection from the south. Turner *et al.* (2009) also mentioned that many strong wind events at Bellingshausen are accompanied by negative temperature anomalies, since the strongest winds around a low often brought cold and more unstable air from the south.

5 | SIMULATION RESULTS OF STRONG WIND EVENT

5.1 | Sensitivity to the initialization time

Figure 7 shows the hourly time series of surface variables resulting from Polar WRF simulations (3 km) initialized at different times at 0000 UTC from 1 to 6 January and considering spin-up time of 24 h. The black dots represent hourly mean observations at KSJ. Among them, the simulated wind speed from "jan6" (blue), the model that is initialized 24 h before the occurrence of the strong wind event, is most consistent with observations. Simulated wind speeds generally agree well with the observations, especially during the generation and maintenance phase of the strong wind on 7 January. The wind speed, which is approximately 8.6 m/s at 0000 UTC 7 January, rapidly increases and reaches its maximum value of ~21 m/s at 0800 UTC, and remains at this level until 1800 UTC in observations. The simulated wind speed from "jan6" captures the variation of this strong wind well, in terms of strength (overestimate by 14% of the wind speed at 0000 UTC and underestimate by 4% of the wind speed at 0800 UTC) and abrupt transition of the wind speed. Among the remaining experimental results, "jan5" which is initialized on 5 January, two days before the occurrence of the strong wind event, simulates wind speed that is relatively consistent with observations. However, the peak wind speed is slightly

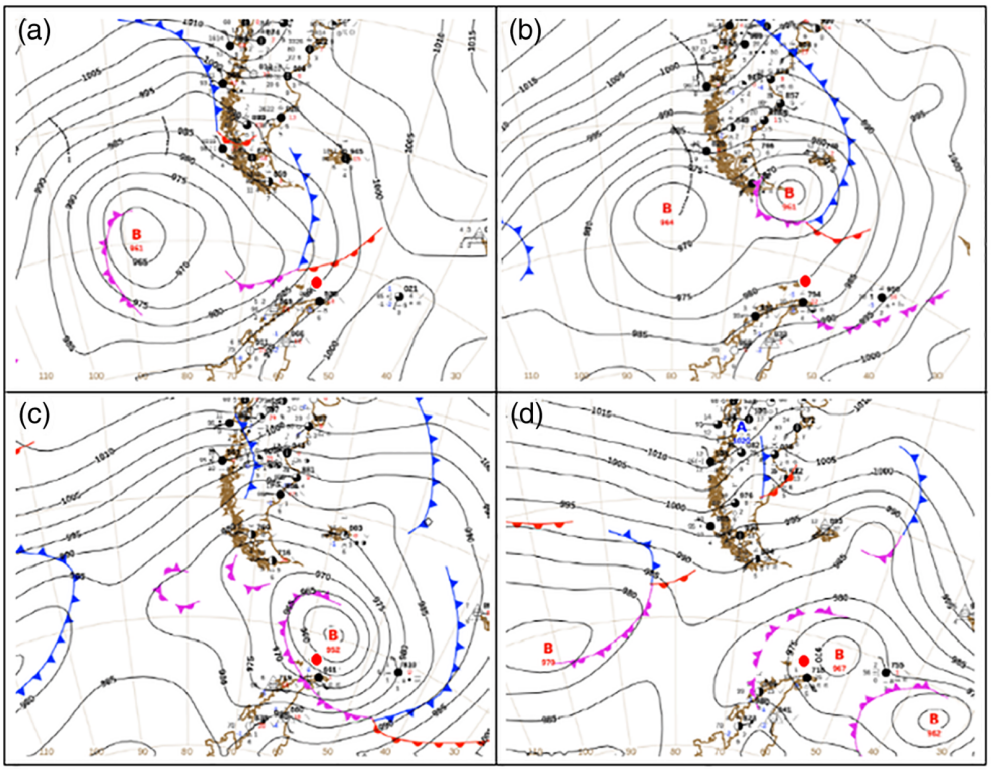

FIGURE 6 Surface weather maps at: (a) 0000 and (b) 1800 UTC on 6 January 2013; (c) 1800 UTC 7 January 2013; and (d) 1800 UTC 8 January 2013, obtained from the Chilean Meteorological Office. Sea-level pressure (solid black lines) is shown at 4 hPa intervals. The warm (red) and cold (blue) fronts are shown. The KSJ station at King George Island is also indicated (red circle) [Colour figure can be viewed at wileyonlinelibrary.com].

underestimated compared to the observation. Simulations initialized before 0000 UTC 4 January underestimate the peak wind speed by around 30% and poorly represent the timing of the wind speed shift. The simulation result from "s24h" shows a similar wind speed to those from "jan6" on 6 and 7 January. Note that the simulated wind speeds on 7 January from "s24h" are the same as those from "jan6", but they start to diverge from "jan6" and observations at 0000 UTC 8 January. This division comes from the difference between the simulation results after 24 h from 0000 UTC 7 January from "s24h" and after 48 h from 0000 UTC 6 January from "jan6".

Similar to wind speed, all experiments are able to capture temporal variation of the sea-level pressure (Figure 7b). "jan6" again shows the most consistent match with the observed sea-level pressure, except for the period when the sea-level pressure gradually decreases from 0000 to 0600 UTC on 7 January. The observed sea-level pressure minimum, with the value of ~962 hPa at 1600 UTC 7 January, is well reproduced by "jan6" with the value of ~963 hPa. Other experiments show minimum pressures that are slightly lower than observations, by about 2–3 hPa ("jan2" show the lowest value of ~958 hPa).

Compared to other surface variables, the simulated 2 m temperatures from all the experiments show relatively large differences from the observations, especially on 6 January (Figure 7c). In general, the model simulations tend to overestimate 2 m temperature. However, interestingly, the 2 m temperature simulated by "jan6" is in a good agreement with the observation for the period from 0200 to 1500 UTC on 7 January, when the strong wind is generated and maintained.

All model simulations show a good representation of the southeasterly winds (110–150°) during the maintenance phase of the strong wind on 7 January (Figure 7d). Statistics showing simulation performance of sensitivity experiments are presented in Figure 8. As expected, the "jan6" experiment outperforms and shows the best statistics among experiments for wind speed, 2 m temperature and sea-level pressure.

5.2 | Strong wind event simulated by Polar WRF

To look into the mechanism of the strong wind event, the wind field and low-pressure system around KSJ are examined. Only the simulation result from "jan6", which shows the best performance, is presented. Figure 9 shows the evolution of the large-scale features of the 3 km domain sea-level pressure with wind vectors at three stages of the strong wind event, the onset (0000 UTC 7 January), the strongest (0800 UTC 7 January), and the cessation phase (1200 UTC 8 January). At the onset (Figure 9a), an edge of the simulated low-pressure system spanning King George Island and the vicinity of KSJ is affected by the associated easterly wind (~100°). At the strongest phase (Figure 9b), the low-pressure system develops and moves southeastwards, causing a decrease in surface pressure and an increase in the wind speed near KSJ as time goes by. The isobar distribution is denser and the easterly wind turns into a stronger southeasterly wind (~130°) around

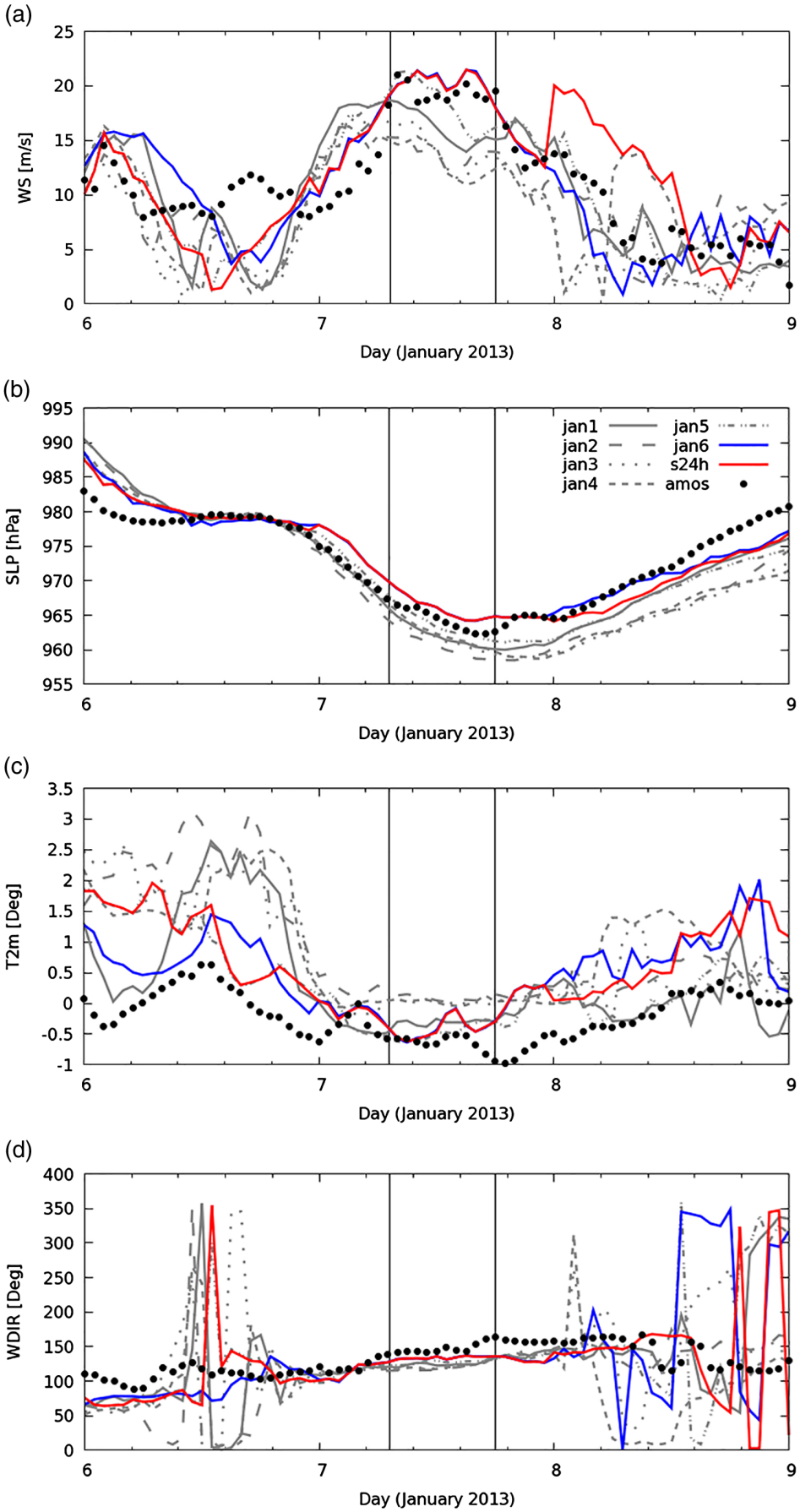

FIGURE 7 Hourly time-series of (a) 10 m wind speed (m/s); (b) sea-level pressure (hPa); (c) 2 m air temperature (°C) and (d) wind direction (degrees) from AMOS and Polar WRF simulations (3 km) with different initialization times (jan1–jan6) and consideration of spin-up time of 24 h (s24h). The solid vertical lines indicate the strong wind period from 0700 to 1800 UTC on 7 January [Colour figure can be viewed at wileyonlinelibrary.com].

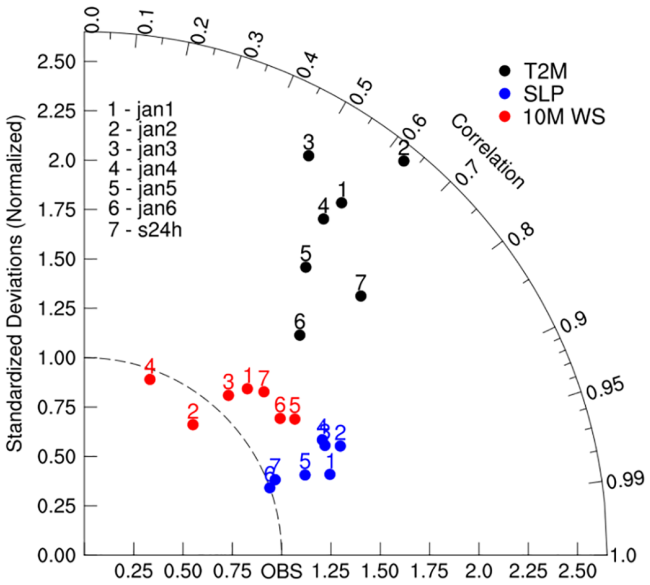

FIGURE 8 Taylor diagram showing model simulation skills of 10 m wind speed (red filled circle), sea-level pressure (blue filled circle), and 2 m air temperature (black filled circle) relative to the observations at KSJ station. The numbers from 1 to 7 represent model experiment with different initialization times [Colour figure can be viewed at wileyonlinelibrary.com].

KSJ. At 0800 UTC on 8 January, when a relatively weak wind is observed at KSJ, the low-pressure system has moved farther southeast and the intensity of the centre pressure becomes weaker and the wind direction also changes consistently with the location of the low-pressure system (Figure 9c).

The change of the wind field around KSJ along with the evolution of the low-pressure system can be seen more clearly in the enlarged view of the model simulation (Figure 10a–d). At 0000 UTC 7 January, there exists a weak easterly with the wind speed of less than ~10 m/s around KSJ (Figure 10a). At the strongest phase, strong southeasterly winds with a speed of more than ~20 m/s are well represented from west of the AP towards King George Island, and KSJ is obviously under the influence of the strong wind (Figure 10b). It should be noted that the strong wind appears on the lee side of the AP with the acceleration of its speed at the downstream region towards KSJ at the peak phase. Acceleration of the wind on the lee slope of the AP indicates the formation of a downslope windstorm. In this case-study, the downslope windstorm seems to be caused by interaction between the southeasterly flow circumventing the cyclone and topography of the AP upstream of KSJ. As the cyclone approaches the AP, the isobaric lines of sea-level pressure become tighter and are deformed around the AP due to the topography. There is a strong discontinuity of the isobars along the east coast of the AP. Notably, a southeasterly wind is formed over the east coast area of the AP and this wind direction is different from the average wind direction in other regions (Figure 10c,d).

The intensification of pressure gradient perpendicular to the coastal line of the AP leads to speed-up of the local flow across the mountain barrier. To help understand the process of accelerated wind, the Froude number is calculated using some representative values from the model output (Table 2). The Froude number used in this study is:

$$Fr = U_0\left(gH\frac{\Delta\theta}{\theta}\right)^{-1/2},$$

where U_0 is the wind speed, g is the gravitational acceleration (9.8 m/s^2), H is the height of the obstacle, $\Delta\theta$ is the increase in potential temperature of the layer between the surface and the top of the obstacle, and θ is the average potential temperature of the layer between the surface and the height of the obstacle (O'Connor and Bromwich, 1988). Froude numbers substantially increase from 1.8 at 0000 UTC to 3.7 at 0800 UTC at the windward side of the AP. $Fr > 1$ indicates that the flow will have sufficient kinetic energy to traverse the topography. That is, continuous flow overriding the AP, under conditions where Fr is greater than one, is important for development of the downslope windstorm in this case. Downslope winds are known to be caused by a hydraulic jump (Long, 1953; Durran, 1990), partial reflection of upward-directed wave energy toward the ground (Klemp and Lilly, 1975) and critical level reflection (Clark and Peltier, 1984). Further quantitative

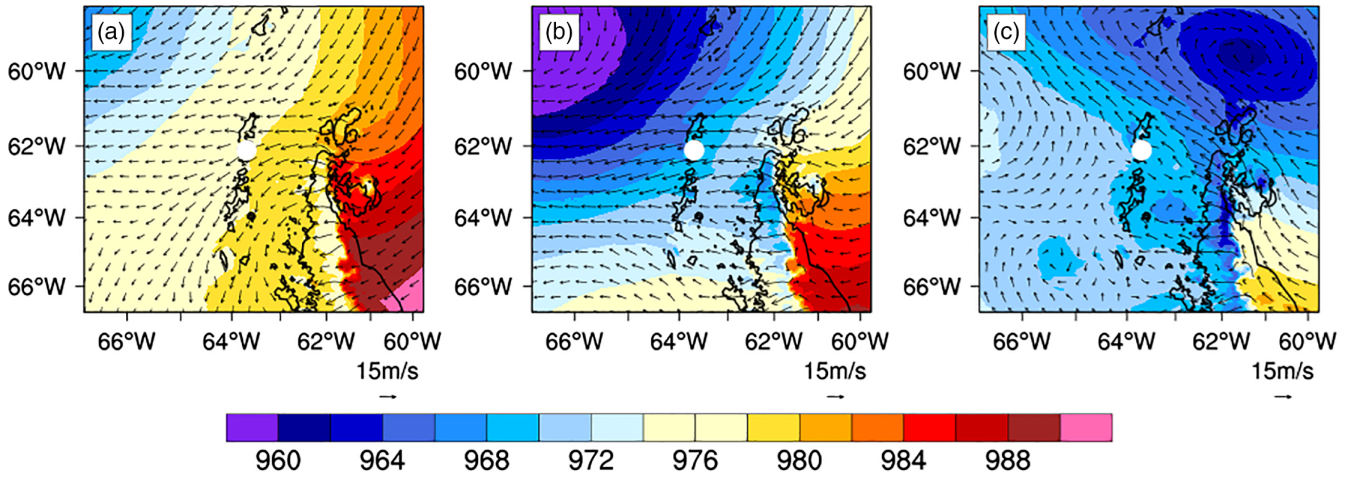

FIGURE 9 Sea-level pressure (shading, 2 hPa interval) with wind vectors at (a) 0000 and (b) 0800 UTC 7 January 2013, and (c) 0900 UTC 8 January 2013 from Polar WRF simulation ("jan6") with 3 km grid resolution. KSJ station is indicated by filled white circle

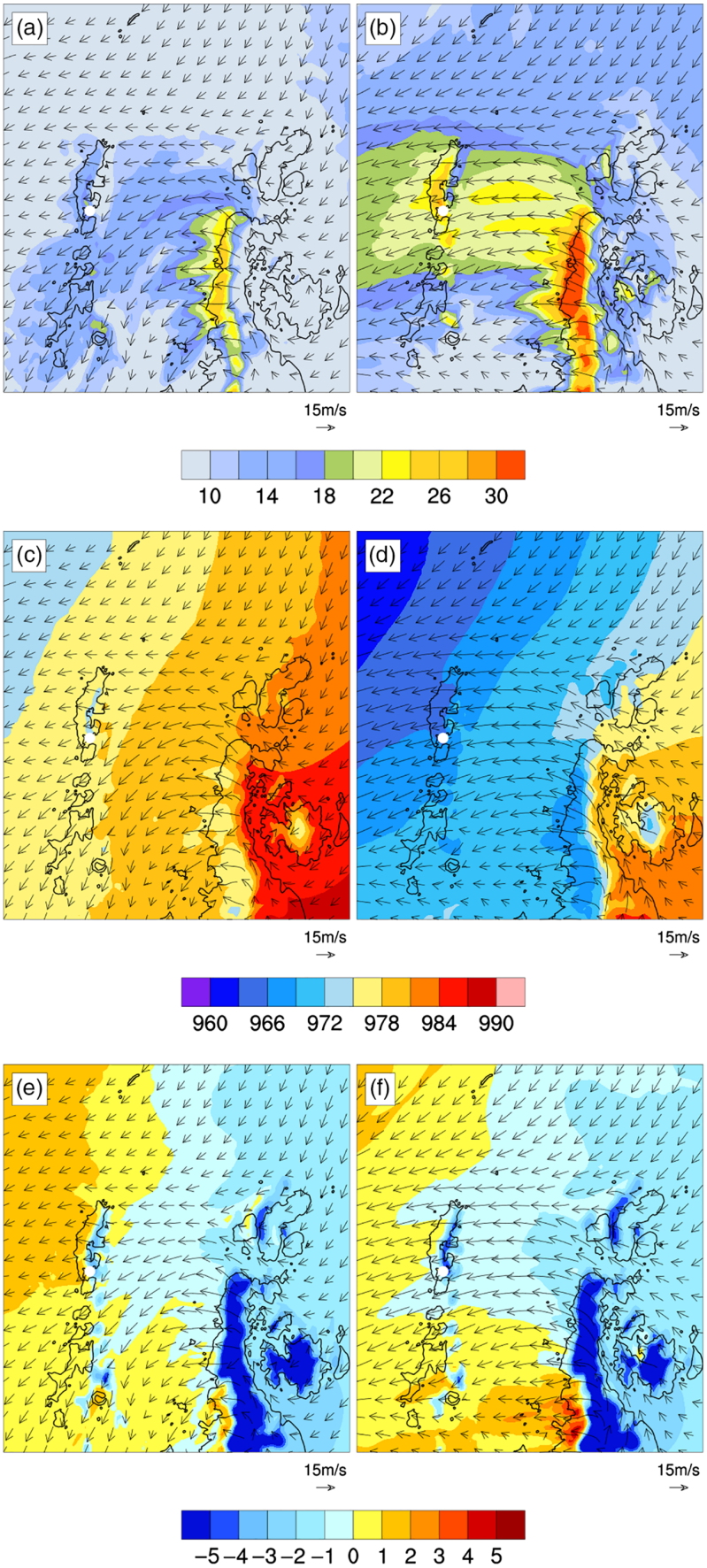

FIGURE 10 (a,b) Wind speed (shading, 2 m/s interval), (c,d) sea-level pressure (shading, 3 hPa interval), and (e,f) 2 m air temperature (shading, °C) with wind vector for a zoomed region over the KSJ station at (a,c,e) 0000 and (b,d,f) 0800 UTC on 7 January 2013 from Polar WRF simulation ("jan6") with 3 km grid resolution. KSJ is indicated by a white circle [Colour figure can be viewed at wileyonlinelibrary.com].

TABLE 2 Froude number and used representative value of model output in Froude number calculation at 0000 and 0800 UTC 7 January 2013

	0000 UTC	0800 UTC
H	515 m	515 m
U_0	10 m/s	16 m/s
θ	268.2 K	268.5 K
$\Delta\theta$	1.6 K	1.0 K
Froude number	1.8	3.7

analysis of the generating mechanism is beyond the scope of this article.

To further examine whether this strong wind case can be regarded as a typical downslope windstorm, we check the vertical structure of the wind for the same period. Figure 11 shows the vertical cross-section of horizontal wind with potential temperature at 0000 and 0800 UTC on 7 January along the line from A to B shown in Figure 1b. The potential temperature shows a wavy structure over the AP and the horizontal wind speed shows a maximum core on the lee side of it. On the other hand, there is a relatively weak wind on the windward side. The vertical structure of the potential temperature and wind fields in Figure 11b has a qualitative resemblance to those seen in a previous study of downslope windstorms over Minna Bluff and Black Island of the Ross Ice Shelf (Steinhoff *et al.,* 2008). Note that a core of high wind speed on the lee side of the AP extends to near King George Island. This indicates that besides the approach of the low-pressure system, topography of the AP acts as an additional forcing to produce a downslope windstorm and eventually strong winds at KSJ.

Figure 10e,f show the temperature fields during the strong wind events. As the southeasterly wind becomes stronger, the cold air in the Weddell Sea and the AP is advected towards King George Island, where KSJ is located. The temperature decrease during the strong wind event shown in the simulated 2 m temperature time series (Figure 7c) can be explained by this cold advection.

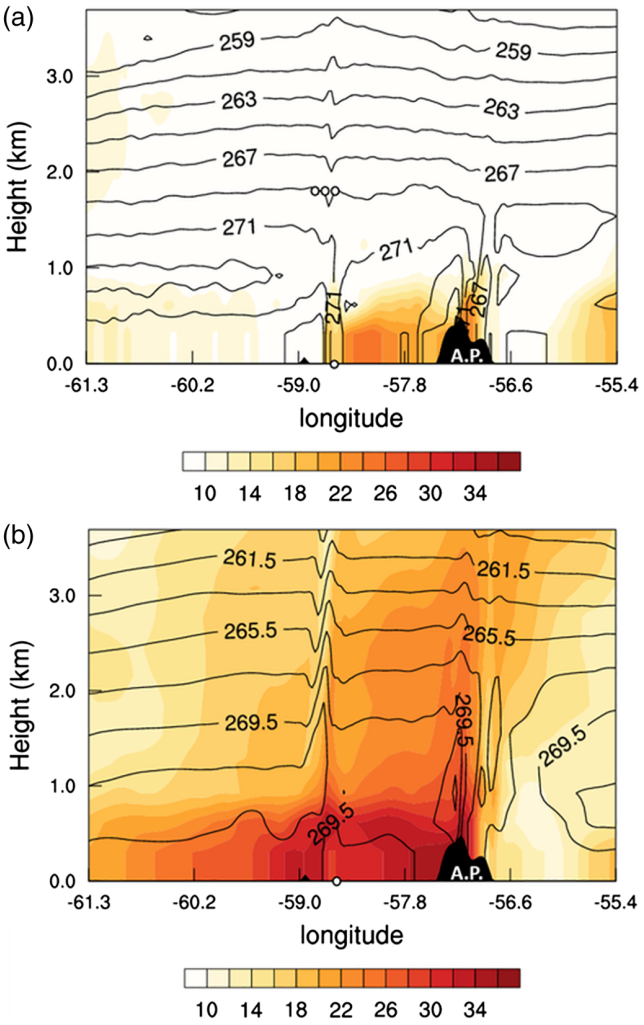

FIGURE 11 Vertical cross-section of potential temperature (contour, 2 K interval) and horizontal wind speed (shading, 2 m/s interval) along the line from A (left corner on x-axis) to B (right corner on x-axis) shown in Figure 1b at (a) 0000 and (b) 0800 UTC on 7 January 2013. White circle indicates the KSJ station. A.P. indicates the Antarctic Peninsula [Colour figure can be viewed at wileyonlinelibrary.com].

5.3 | Sensitivity to the modelled horizontal resolution

Since the "jan6" simulation resulted in the best match between modelled and observed data, the sensitivity of strong wind simulation to the horizontal resolution is examined based on the "jan6" configuration. The use of two-way nesting in "jan6" cannot provide a fair view of the effect of model horizontal resolution on the simulation, because the components of the resolved features in the inner domain are fed back to the outer domain, providing high-resolution information to the outer domain. To prevent this, we resolve the resolution issue using one-way nesting. Figure 12 shows model simulation skills of 10 m wind speed, sea-level pressure and 2 m air temperature with different horizontal resolutions from two-way nesting experiments.

In the two-way nesting experiment, the model output shows little sensitivity to the horizontal resolution (Figure 12a). However, in one-way nesting, the 27 km simulation of the strong wind event shows a poor performance for wind speed and sea-level pressure, different from 3 and 9 km model simulations (Figure 12b). The 3 and 9 km model experiments simulate 95% of the maximum wind speed (maximum hourly wind speed of ~21 m/s at 0800 UTC 7 January), whereas the 27 km model underestimates the peak wind speed by around 44%. Similarly, the 27 km model underestimates the minimum sea-level pressure by ~3 hPa (~962 hPa) at 1600 UTC 7 January. The simulated 2 m temperatures show a large difference among the experiments of different horizontal resolutions compared to other variables. Overall, the strong wind simulations are sensitive to the horizontal resolution in a one-way nesting experiment and the 27 km model experiment shows a poor performance, which is not suitable for the simulation of the strong wind event in this study.

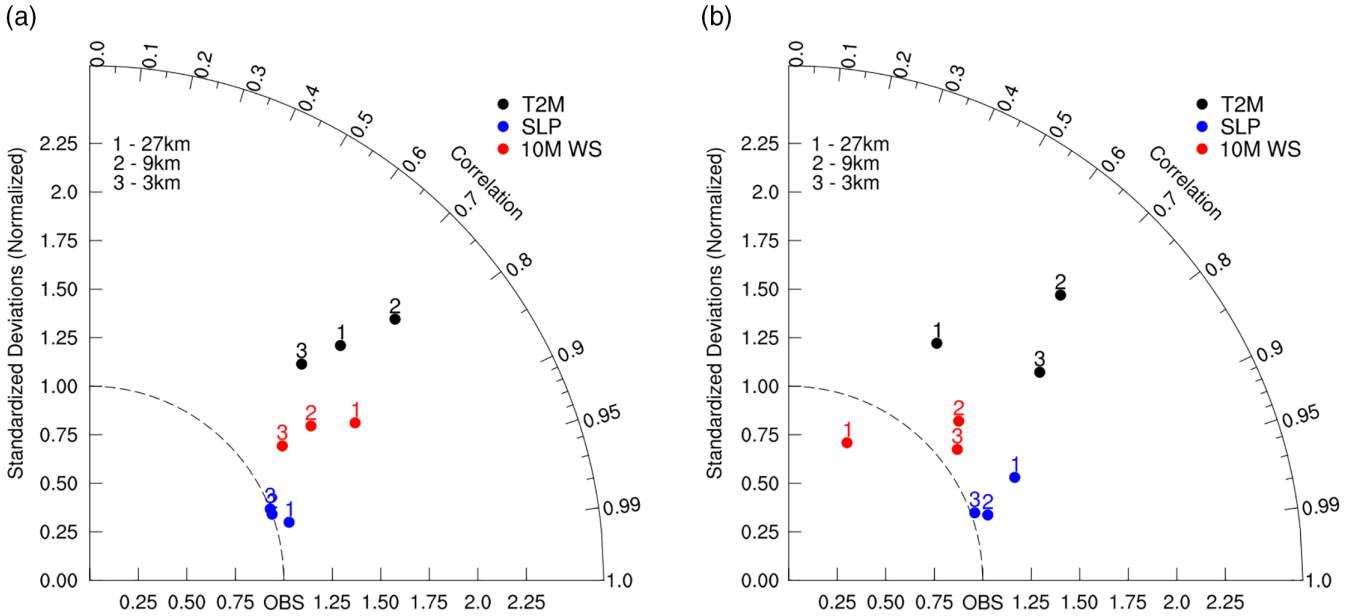

FIGURE 12 Taylor diagram showing model simulation skills for 10 m wind speed (red circle), sea-level pressure (blue circle) and 2 m air temperature (black circle) with different horizontal resolutions relative to the observation at KSJ station. (a) and (b) represent the model results for two-way and one-way nesting, respectively. The numbers from 1 to 3 represent different horizontal resolutions [Colour figure can be viewed at wileyonlinelibrary.com].

6 | SUMMARY AND DISCUSSION

In this study, we investigate the strong wind event occurring at Antarctic station King Sejong (KSJ) on 7 January 2013 using the station observations, reanalysis, and a series of model simulations. The observed maximum value of the 10 min wind speed was 21.9 m/s, and classified as a "severe gale" in the Beaufort wind force system. Maximum instantaneous wind speed also reached an extreme value of 41 m/s.

We first analyse the climatological characteristics of the wind speed of the 27-year period (1989–2015) observed at KSJ to assess the degree of extremity for the selected strong-wind case. From the analysis of wind frequency distribution using station data at KSJ, we show that the chosen strong-wind case is extremely rare in summer. The values of 10 min averaged and maximum instantaneous wind speed during this storm occur less than 0.34% and 0.8% of the time in the frequency histograms of wind speed at KSJ, respectively.

To examine the characteristics of extreme wind events at KSJ, we investigated 22 strong-wind cases belonging to instantaneous wind speed over 41 m/s, which is less than 1% of the observed winds. The strong-wind case shows the bimodal distribution of maximum instantaneous wind speeds with wind directions of easterly and northerly, dependent on the location of the cyclone. Notably, we could confirm that the existence of a well-developed low-pressure system passing by Drake Passage was a common important factor for the strong wind event at KSJ.

The simulation results initialized at 0000 UTC 6 January 2013, the day prior to the occurrence of the strong wind event, produce the most accurate representation of the wind speed (~94% of the peak wind speed). The model simulations confirm that the selected strong wind event is due to the approach of an intense synoptic-scale low-pressure system. The model successfully simulates the low-pressure system generated at the southernmost part of Chile, which then gradually develops and moves southeastward to the vicinity of King George Island, maintaining its strong intensity on 7 January. The existence of the topography at the AP near KSJ plays a role in intensifying the wind with a deformation of the flow pattern originally configured by the low-pressure system approach. As the cyclone approaches the AP, the sea-level pressure isobars become denser and deformed around the AP due to the topography. This condition results in a strong discontinuity of the isobars along the east coast of the AP, and a southeasterly wind is formed over the eastern coastal area of the AP. The intensified pressure gradient, perpendicular to the coastal line of the AP, leads to speed-up of the local flow across the mountain barrier with time. KSJ station located on the lee side of the AP is under the influence of the strong southeasterly wind. In addition, the continuous flow overriding the AP accelerates wind (downslope windstorm) on the lee side, and eventually a core of high wind speed extends to KSJ. This implies that the topography of the AP provides additional forcing for strong winds at KSJ. Additional model experiments might be needed for the quantification in the future.

The sensitivity test on different horizontal resolutions with one-way nesting supports the possibility that variables could be affected by the topography of the AP on strong winds at KSJ. The 3 and 9 km model simulations of strong wind events show a good agreement with the observations, whereas the 27 km model shows remarkably poor performance for the wind speed and sea-level pressure. The 3 and 9 km models well represent the dense and deformed isobar distribution along the east coast of the AP due to the topography at the strong phase of the wind speed, but the 27 km model fails to

represent this sea-level pressure pattern. This suggests that the pressure distribution deformed by the topography of the AP is poorly represented at the 27 km model domain. We conclude that the strong wind event at KSJ on 7 January 2013 is caused by the combined effect of both a synoptic-scale low-pressure system and local topography of the AP near KSJ.

ACKNOWLEDGEMENTS

This study has been conducted with the support of "PE19010" of the Korea Polar Research Institute. We express our sincere thanks to anonymous reviewers and the editor who have examined the article and given advice on many aspects.

ORCID

Seong-Joong Kim https://orcid.org/0000-0002-6232-8082

REFERENCES

Adams, N. (2005) Identifying the characteristics of strong southerly wind events at Casey Station in East Antarctica using a numerical weather prediction system. *Monthly Weather Review*, 113, 3548–3561. https://doi.org/10.1175/MWR3050.1.

Ball, F.K. (1960) *Winds on the ice slopes of Antarctica. Antarctic Meteorology*. London: Pergamon Press, pp. 9–16.

Bromwich, D.H., Otieno, F.O., Hines, K.M., Manning, K.W. and Shilo, E. (2013) Comprehensive evaluation of polar weather research and forecasting performance in the Antarctic. *Journal of Geophysical Research*, 118, 274–292. https://doi.org/10.1029/2012JD018139.

Chen, F. and Dudhia, J. (2001) Coupling an advanced land surface–hydrology model with the Penn State–NCAR MM5 modeling system. Part I: Model implementation and sensitivity. *Monthly Weather Review*, 129, 569–585. https://doi.org/10.1175/1520-0493(2001)129<0569:CAALSH>2.0.CO;2.

Clark, T.L. and Peltier, W.R. (1984) Critical level reflection and the resonant growth of nonlinear mountain waves. *Journal of the Atmospheric Sciences*, 41, 3122–3134.

Deb, P., Orr, A., Hosking, J.S., Phillips, T., Turner, J., Bannister, D., Pope, J.O. and Colwell, S. (2016) An assessment of the Polar Weather Research and Forecast (WRF) model representation of near-surface meteorological variables over West Antarctica. *Journal of Geophysical Research – Atmospheres*, 121(427), 1532–1548. https://doi.org/10.1002/2015JD024037.

Dee, D.P., Uppala, S.M., Simmons, A.J., Berrisford, P., Poli, P., Kobayashi, S., Andrae, U., Balmaseda, M.A., Balsamo, G., Bauer, P., Bechtold, P., Beljaars, A.C.M., van de Berg, L., Bidlot, J., Bormann, N., Delsol, C., Dragani, R., Fuentes, M., Geer, A.J., Haimberger, L., Healy, S.B., Hersbach, H., Hólm, E.V., Isaksen, L., Kållberg, P., Köhler, M., Matricardi, M., McNally, A.P., Monge-Sanz, B.M., Morcrette, J.-J., Park, B.K., Peubey, C., de Rosnay, P., Tavolato, C., Thépaut, J.-N. and Vitart, F. (2011) The ERA-Interim reanalysis: configuration and performance of the data assimilation system. *Quarterly Journal of the Royal Meteorological Society*, 137, 553–597. https://doi.org/10.1002/qj.828.

Durran, D.R. (1990) *Mountain waves and downslope winds. Atmospheric Processes Over Complex Terrain, Meteorological Monographs*, Vol. 45. Boston, MA: American Meteorological Society, pp. 59–81.

Giorgi, F., Brodeur, C.S. and Bates, G.T. (1994) Regional climate change scenarios over the United States produced with a nested regional climate model. *Journal of Climate*, 7, 375–399. https://doi.org/10.1175/1520-0442(1994)007<0375:RCCSOT>2.0.CO;2.

Grell, G.A. and Devenyi, D. (2002) A generalized approach to parameterizing convection combining ensemble and data assimilation techniques. *Geophysical Research Letters*, 29(14), 38-1–38-4. https://doi.org/10.1029/ 2002GL015311.

Heinemann G. (1997) Idealized simulations of the Antarctic katabatic wind system with a three-dimensional mesoscale model. *Journal of Geophysical Research,* 102, 13825–13834. doi:https://doi.org/10.1029/97JD00457.

Hines, K.M. and Bromwich, D.H. (2008) Development and testing of Polar Weather Research and Forecasting (WRF) model. Part I: Greenland ice sheet meteorology. *Monthly Weather Review*, 136, 1971–1989. https://doi.org/10.1175/2007MWR2112.1.

Hong, S.Y., Dudhia, J. and Chen, S.H. (2003) A revised approach to ice-microphysical processes for the bulk parameterization of cloud and precipitation. *Monthly Weather Review*, 132, 103–120. https://doi.org/10.1175/1520-0493(2004)132<0103:ARATIM>2.0.CO;2.

Iacono, M.J., Delamere, J.S., Mlawer, E.J., Shephard, M.W., Clough, S.A. and Collins, W.D. (2008) Radiative forcing by long–lived greenhouse gases: calculations with the AER radiative transfer models. *Journal of Geophysical Research*, 113, D13103. https://doi.org/10.1029/2008JD009944.

Janjić, Z.I. (1994) The step–mountain eta coordinate model: further developments of the convection, viscous sublayer and turbulence closure schemes. *Monthly Weather Review*, 122, 927–945. https://doi.org/10.1175/1520-0493(1994)122<0927:TSMECM>2.0.CO;2.

Klemp, J.B. and Lilly, D.R. (1975) The dynamics of wave-induced downslope winds. *Journal of the Atmospheric Sciences*, 32, 320–339.

Long, R.R. (1953) Some aspects of the flow of stratified fluids. I: A theoretical investigation. *Tellus*, 5, 42–58.

Meehl, G.A. (1991) A reexamination of the mechanism of the semiannual oscillation in the Southern Hemisphere. *Journal of Climate*, 4, 911–925. https://doi.org/10.1175/15200442(1991)004<0911:AROTMO> 2.0.CO;2.

Monin, A.S. and Obukhov, A.M. (1954) Osnovnye zakonomernosti turbulentnogo peremeshivanija v prizemnom sloe atmosfery (Basic laws of turbulent mixing in the atmosphere near the ground). *Trudy geofiz. inst. AN SSSR*, 24(151), 163–187.

O'Connor, W.P. and Bromwich, D.H. (1988) Surface airflow around Windless Bight, Ross Island, Antarctica. *Quarterly Journal of the Royal Meteorological Society*, 114, 917–938.

Orr, A., Phillips, T., Webster, S., Elvidge, A., Weeks, M., Hosking, S.J. and Turner, J. (2014) Met Office Unified Model high-resolution simulations of a strong wind event in Antarctica. *Quarterly Journal of the Royal Meteorological Society*, 140, 2287–2297. https://doi.org/10.1002/qj.2296.

Parish, T.R. and Bromwich, D.H. (1987) The surface windfield over the Antarctic ice sheets. *Nature*, 328, 51–54. https://doi.org/10.1038/328051a0.

Parish, T.R. and Bromwich, D.H. (1998) A case study of Antarctic katabatic wind interaction with large-scale forcing. *Monthly Weather Review*, 126, 199–209. https://doi.org/10.1175/1520-0493(1998)126<0199:ACSOAK>2.0.CO;2.

Parish, T.R. and Waight, K.T. (1987) The forcing of Antarctic katabatic winds. *Monthly Weather Review*, 115, 2214–2226. https://doi.org/10.1175/1520-0493(1987)115<2214:TFOAKW>2.0.CO;2.

Park, S.J., Choi, T.J. and Kim, S.J. (2013) Heat flux variations over sea ice observed at the coastal area of the Sejong Station, Antarctica. *Asia-Pacific Journal of Atmospheric Sciences*, 49(4), 443–450. https://doi.org/10.1007/s13143-013-0040-z.

Powers, J.G., Klemp, J.B., Skamarock, W.C., Davis, C.A., Dudhia, J., Gill, D.O., Coen, J.L., Gochis, D.J., Ahmadov, R., Peckham, S.E., Grell, G.A., Michalakes, J., Trahan, S., Benjamin, S.G., Alexander, C.R., Dimego, G.J., Wang, W., Schwartz, C.S., Romine, G.S., Liu, Z., Snyder, C., Chen, F., Barlage, M.J., Yu, W. and Duda, M.G. (2017) The Weather Research and Forecasting model: overview, system efforts, and future directions. *Bulletin of the American Meteorological Society*, 98, 1717–1737. https://doi.org/10.1175/BAMS-D-15-00308.1.

Simmonds, I. and Jones, D.A. (1998) The mean structure and temporal variability of the semiannual oscillation in the southern extratropics. *International Journal of Climatology*, 18, 473–504. https://doi.org/10.1002/(SICI)1,097-0088(199804)18:5<473::AID-JOC266>3.0.CO;2–0.

Simmonds, I. and Keay, K. (2000) Mean Southern Hemisphere extratropical cyclone behavior in the 40-year NCEP-NCAR reanalysis. *Journal of Climate*, 13, 873–885. https://doi.org/10.1175/1520 0442(2000)013<0873:MSHECB>2.0.CO;2.

Steinhoff, D.F., Bromwich, D.H., Lambertson, M., Knuth, S.L. and Lazzara, M.A. (2008) A dynamical investigation of the May 2004 McMurdo Antarctica severe wind event using AMPS. *Monthly Weather Review*, 136, 7–26. https://doi.org/10.1175/2007MWR1999.1.

Turner, J., Lachlan-Cope, T.A., Marshall, G.J., Pendlebury, S. and Adams, N. (2001) An extreme wind event at Casey Station, Antarctica. *Journal of Geophysical Research*, 106, 7291–7311. https://doi.org/10.1029/2000JD900544.

Turner, J., Colwell, S.R., Marshall, G.J., Lachlan-Cope, T.A., Carleton, A.M., Jones, P.D., Lagun, V., Reid, P.A. and Iagovkina, S. (2004) The SCAR

READER project: toward a high-quality database of mean Antarctic meteorological observations. *Journal of Climate*, 17, 2890–2898. https://doi.org/10.1175/1520-0442(2004)017,2,890:TSRPTA.2.0.CO;2.

Turner, J., Chenoli, S.N., Samah, A., Marshall, G.J., Phillips, T. and Orr, A. (2009) Strong wind events in the Antarctic. *Journal of Geophysical Research*, 114, D18103. https://doi.org/10.1029/2008JD011642.

van den Broeke, M.R. and van Lipzig, N.P.M. (2003) Factors controlling the near surface wind field in Antarctica. *Monthly Weather Review*, 131, 733–743. https://doi.org/10.1111/j.1600-0870.2010.00443.x.

van Wessem, J.M., Reijmer, C.H., van de Berg, W.J., van den Broeke, M.R., Cook, A.J., van Ulft, L.H. and van Meijgaard, E. (2015) Temperature and wind climate of the Antarctic peninsula as simulated by a high-resolution regional atmospheric climate model. *Journal of Climate*, 28, 7306–7326. https://doi.org/10.1175/JCLI-D-15-0060.1.

How to cite this article: Kwon H, Park S-J, Lee S, Kim B-M, Choi T, Kim S-J. A numerical simulation of a strong wind event in January 2013 at King Sejong station, Antarctica. *Q J R Meteorol Soc* 2019;145:1267–1280. https://doi.org/10.1002/qj.3496